ORIGINAL PAPER

Surface Dielectric Barrier Discharge (sDBD) for Flow Control in Plasma Conversion

Soad Mohsenimehr[1] · Achim von Keudell[1]

Abstract

Dielectric barrier discharges (DBD) are often used for gas conversion, such as carbon dioxide splitting, volatile organic compound removal or ozone generation. Due to the tiny plasma filaments in DBD discharges, efficient mixing of the gas flow with the plasma is essential. This is studied by using a surface dielectric barrier discharge (sDBD) with an electrode design similar to plasma actuators to optimize plasma-flow interaction. The flow pattern has been measured by Schlieren diagnostics and compared to a fluid dynamic simulation. Gas conversion efficiency has been tested by monitoring the conversion of 0.7% CO_2 admixed to an N_2 gas stream via infrared spectroscopy in the exhaust. The actuator design of the electrodes induces a significant plasma force on the fluid, which results in the formation of vortices above the electrodes, as reproduced in the simulation. It is shown that the height of the vortices created in the velocity field can characterize the mixing process, which dominates the conversion efficiency of carbon dioxide at different gas flow rates.

Keywords Surface dielectric barrier discharge · Flow pattern · Vortex formation · Schlieren imaging

Introduction

Dielectric Barrier Discharges (DBD) are well-known plasma sources for gas conversion due to their easy scalability and flexibility for various applications [1, 2]. Different configurations of DBDs have been used for CO_2 splitting to enhance the efficiency of conversion by varying electrode material and design, including packed materials in different shapes and sizes or adding catalyst in contact to the plasma [3–6]. Removal of volatile organic compounds (VOC) from a gas stream is another challenge in gas conversion by plasma and has been investigated by so-called surface DBDs [7, 8]. The electrodes of a surface DBD (sDBD) are placed on the same dielectric so that the volume to be treated can be very large in comparison to a volume DBD (vDBD) where the electrodes and dielectrics are placed opposite to each other at a distance of typically only 1 mm. Schücke et al. performed experiments using so-called twin sDBD, consisting of grid lines as electrodes on directly both

✉ Soad Mohsenimehr
Soad.Mohsenimehr@rub.de

1 Experimental Physics II - Reactive Plasmas, Ruhr-Universität Bochum, 44780 Bochum, Germany

sides of a dielectric plate, creating thereby two surface discharges within the electric stray field in a large gas volume [9, 10]. This has the advantage that the pressure drop along the gas stream is very small in comparison to a volume DBD (vDBD), where the pressure drop is large since the gas has to pass a small gap in between the electrodes. Any large pressure drop would limit the absolute gas flow or require elaborate pumping concepts to treat large gas volumes. Schücke et al. also monitored the density of reactive species in such twin sDBDs and their role in the conversion of n-butane in air by using optical absorption spectroscopy as well as electrical characterization of the microsecond pulse generator showing an efficient VOC removal. Nguyen-Smith et al. studied the electrode erosion of these sDBD in operation. They compared a microsecond and a nanosecond pulse generator [11] to evaluate the durability of the design for long-term use. The scale-up of this sDBD has been studied by Böddecker et al. [12] by combining 5 electrodes in parallel to treat up to 500 slm of gas. The flow characteristic inside these sDBD has been investigated using the Schlieren imaging technique to analyze the flow pattern and assess the conversion as it depends on the gas flow and the plasma chemistry [13].

These experiments revealed that the gas conversion in these sDBD can be very large despite the fact that the plasma is located at the very electrode surface and fills the gas volume only to a minimal extent. It has been observed [13] that the sDBD exerts a force on the gas, which induces a distinct flow pattern that leads to an efficient mixing of the gas and plasma species. This plasma-induced flow was triggered by the ion wind generated by the electric stray fields. In this paper, we aim to optimize this gas mixing by choosing a different electrode design that is derived from plasma actuators where the opposing electrodes are intentionally displaced from each other. Aerodynamic plasma actuators often include an exposed and an encapsulated electrode with a surface discharge expanding along the dielectric surface [14]. The streamers propagate along the surface, accelerating the ions and neutrals, thereby creating a thrust onto the gas. Many versatile electrode configurations are used as plasma actuators to generate thrust and to manipulate, thereby, the flow pattern, to for example, reduce the drag on an airfoil by controlling the transition from laminar to turbulent flow [15]. Sato et al. [16] proposed unidirectional surface discharges to accelerate an ion wind, which allows enhanced aerodynamic performance. The stabilization of the surface discharge can be achieved by adding a third electrode which is usually biased by a DC voltage that increases the propagation length of the plasma on the surface. This is coined sliding discharge[17].

This work aims to visualize the fluid flow in an optimized actuator design of an sDBD electrode configuration using the Schlieren technique [18]. This method is sensitive to the gradients in the refractive index and, therefore, to the concentration of the species in the plasma, as these determine the refractive index of the medium. The gas conversion efficiency is then assessed by analyzing the dissociation of the test molecules CO_2 seeded to a defined N_2 gas stream.

Experiment

Plasma Reactor

The sketch of the experimental setup is depicted in Figs. 1 and 2. A twin sDBD is employed, which consists of an aluminum oxide plate ($190 \times 88 \times 0.63$ mm) that is covered by nickel grids in a comb design with 10 mm electrode width and 10 mm gap distance
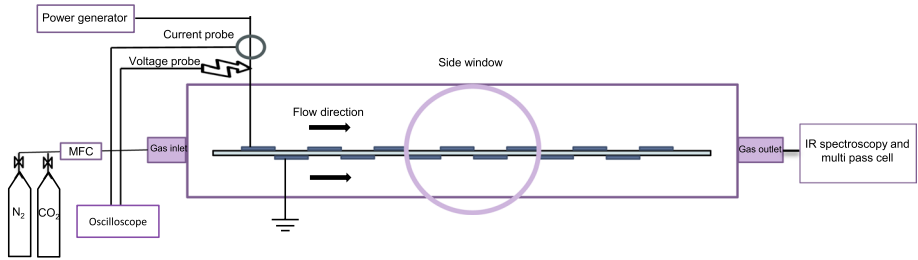
Fig. 1 Cross section of the experimental setup

Fig. 2 **a** Photograph of the electrode (top view); **b** schematic of the plasma operation (side view), **c** photograph of the plasma in operation (side view), dashed lines show the oversized coated electrodes. **d** Simulation domain
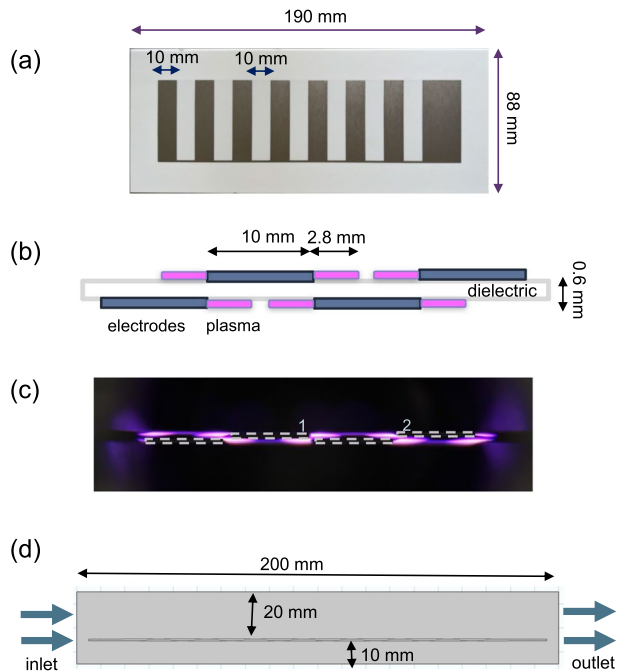
between the electrodes that are printed on both sides and offset from each other by 10 mm (Fig. 2a). This yields an alternate electrode pattern, as illustrated by the cross-section in Fig. 2b. This asymmetric actuator design of the nickel electrodes was chosen to extend the length of the surface discharges along the dielectric surface due to an electric field distribution defined by the grounded nickel counter electrode on the opposite side of the dielectric.

The twin sDBD is placed inside a stainless steel chamber with an inner height of 30 mm (20 mm above and 10 mm below the sDBD) and a width of 120 mm at atmospheric pressure. Damped sinusoidal high voltage bursts with a microsecond rise time are applied at the nickel electrodes (marked as dashed yellow rectangles in the images in Fig. 2c) generated by an external transformer (G2000 Redline Technologies, Germany). The frequency of these bursts is a few 100 kHz at a repetition frequency of 4 kHz. Typical peak-to-peak voltage V_{pp} values range from 6 kV to 11 kV. The discharges ignite along the dielectric surface and by increasing the voltage, the area where the surface streamers propagate along the

sDBD surface is extending. The surface discharges expanding from the electrodes (indicated by 1 and 2 in Fig. 2c) may also meet each other at a certain power, which is expected to enhance the gas mixing in the reactor even further. Nitrogen has been used as the main gas with a purity of 99.999 % at flow rates of 1 slm, 2 slm and 5 slm with an admixture of 1% of carbon dioxide according to the flow controller setting. However, the quantification of CO_2 in the exhaust revealed an actual mixing level of only 0.7% caused by the particular design of the gas mixing panel. The mean flow velocities of 0.004 m/s, 0.009, and 0.023 m/s in the setup when dividing the volume flow by the cross-section of the chamber. The simulation domain is shown in Fig. 2d.

Electrical Characterization

A high-voltage probe (P-6015) and a current monitor (Pearson, model 8590C,V/A1.0) have been used to measure the voltage and current on the powered electrode. A typical current and voltage waveform is shown in Fig. 3a for an experiment using 8 kV peak-to-peak voltage and 1 slm of nitrogen plus 10 sccm CO_2 flow. The average absorbed power $\langle P \rangle$ has been calculated by the following equation:

$$\langle P \rangle = f \int_T U_{\text{meas}} \left(I_{\text{meas}} - C_{\text{sys}} \frac{dU_{\text{meas}}}{dt} \right) dt \tag{1}$$

with the measured current and voltage I_{meas}, and U_{meas}, respectively. C_{sys} denotes the capacitance of the sDBD without the plasma. The latter is extracted directly from fitting a sin wave corresponding to the system current without the plasma I_{system} to the later part of the current waveform after a specific time after the pulse (marked as a vertical dashed green
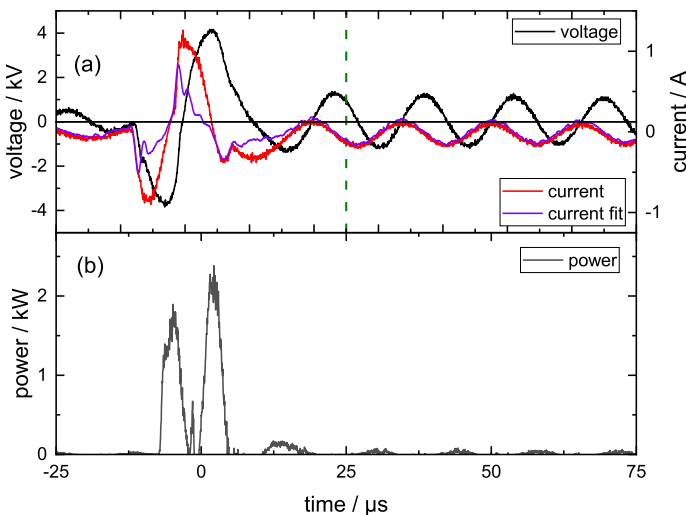
Fig. 3 (a) Typical current and voltage waveform for a plasma operated at $V_{pp} = 8$ kV at a flow of 1 slm nitrogen and 10 sccm CO_2. The system current is the displacement current of the setup with no plasma characterized by a capacitance of 280 pF. (b) Dissipated power over time. The time-averaged power yields 47.95 W (Color figure online)

line in Fig. 3a) yielding approximately $C_{sys} = 280$ pF. The time-resolved power per pulse is plotted in Fig. 3b. One can see that the plasma ignites only for a few cycles of the 100 kHz voltage bursts. The time-averaged power yields 47.95 W.

Infrared Spectroscopy

CO_2 is detected inside the reactor by its infrared absorption signature measured by a Bruker Vertex 70V Fourier transform infrared spectrometer equipped with a variable multipass cell (0.8–8.0 m) as sampling compartment at a temperature of 25 °C. The second harmonic of the asymmetric stretching vibration of CO_2 in the range of 4800–5175 cm^{-1}, CO and N_2O have been observed at 2050–2175 cm^{-1} and at 1240–1330 cm^{-1}, respectively. At first, the reactor is evacuated and then filled with nitrogen at atmospheric pressure. The multipass cell is connected to the outlet of the reactor and a reference background spectrum is taken with pure nitrogen. For the actual measurement, the total flow of N_2 and CO_2 has been varied by keeping the CO_2 admixture at 0.7%. Each concentration was measured after 15 min so that the plasma conversion and the species transport from the reactor to the multipass cell reached an equilibrium. Spectrum fitting and data evaluation has been performed using the HITRAN database and the Beer–Lambert law [19, 20].
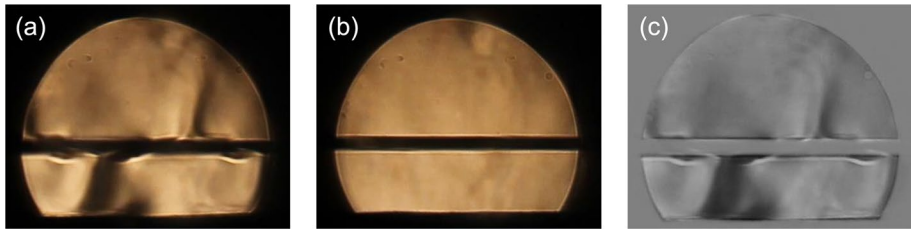
Schlieren Diagnostic

A single mirror Schlieren optical setup was built to visualize the gradient of the refractive index of the medium, as illustrated in Fig. 4. The optical system to analyze the flow pattern is designed as follows: a halogen lamp is focused with a lens ($f = 50$ mm) on a pinhole, creating a point light source. This light then propagates towards a beam splitter. One part passes through the sDBD, reaches a spherical mirror (with a focal length of 1150 mm), is reflected through the plasma, and is split by the beam splitter again. The image of the pinhole is then focused onto a knife edge (which is placed in a normal direction with respect to the sDBD electrode surface) before it is recorded by a digital camera (Canon EOS 60D) ISO speed 120 and an exposure time of 1/100 s.

The analysis of the images is performed as illustrated in Fig. 5. At first, a background image (Fig. 5b) is recorded when there is no plasma and gas flow in the chamber. Then,
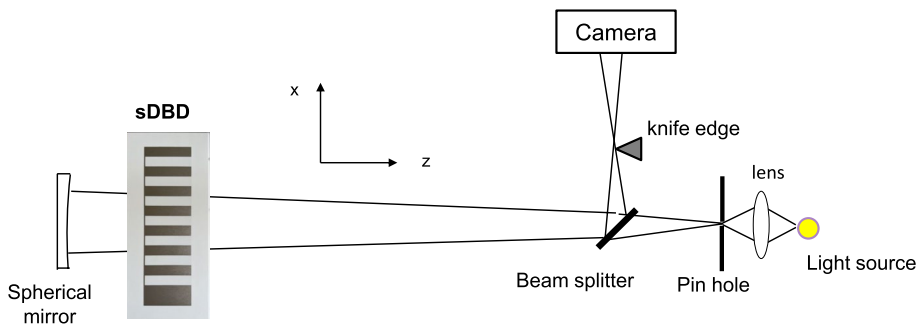
Fig. 4 Schematic of the Schlieren diagnostic used in this work

Fig. 5 Example Schlieren diagnostic: **a** Schlieren image of plasma in 1 slm N_2 at V_{pp} = 10 kV, **b** Schlieren image plasma off, **c** difference image, gray-scale

the image of the plasma (Fig. 5a) is taken at different operating parameters. Finally, the background image is subtracted from the plasma image and converted to a gray scale yielding the actual Schlieren image (Fig. 5c).

Modeling

2d fluid simulations have been performed using COMSOL to predict the behavior of the plasma aerodynamic. The model solves Navier Stokes equations on a mesh assuming compressible laminar flow and small Reynolds numbers. A 2d cross-section of the electrode inside the chamber is defined with a chamber height of 30 mm and a dielectric thickness of 0.63 mm, and the height of the comb electrodes is 0.05 mm. A sketch of the simulation domain is shown in Fig. 2d. The gas flow enters on the left side of the domain and exists on the right side. The slight heating of the electrode during plasma operation is taken into account by setting the surface temperature to 340 K. The gas flow is considered to be pure nitrogen at different mean flow velocities in the simulation, depending on the gas flow rate in the experiment. For simplicity, the effect of the surface discharges on the gas flow has been substituted by a volume force in a defined volume (2d cross-section with a width of 2.8 mm and a height of 0.05 mm in front of the electrodes) with a direction pointing away from the electrode edges as illustrated in Fig. 2b. This is a typical approach for simulating plasma actuators [21–23]. In principle, also a plasma model could be employed to actually calculate the ion wind as the propagating streamers accelerate it. This ion wind then exerts a force on the neutrals and induces a thrust on the flow. Such a model is beyond the scope of this paper. Since the plasma is much smaller than the reactor volume, a simple volume force in a small region is sufficient to describe the plasma's impact on the flow pattern. The absolute value of this volume force is, however, arbitrary and is only chosen to reach a match between the simulated and the measured flow patterns.

An example of this fluid simulation is shown in Fig. 6 for high and low mean flow velocity. One can see the creation of a very distinct flow pattern with vortices being formed that are attached to the electrodes and being pushed by the incoming flow toward the outlet.

The fluid simulation yields a velocity field and a density distribution of the gas in the reactor. From this, artificial Schlieren images are calculated to be compared with the experiment. We use the refractive index of the plasma medium as

$$n = 1 + \frac{1}{4\pi\epsilon_0}2\alpha_+(\lambda)\rho_+ + \frac{1}{4\pi\epsilon_0}2\alpha_n(\lambda)\rho_n - \frac{1}{4\pi\epsilon_0}\frac{e^2\lambda^2}{2\pi m_e c_0^2}\rho_e \tag{2}$$
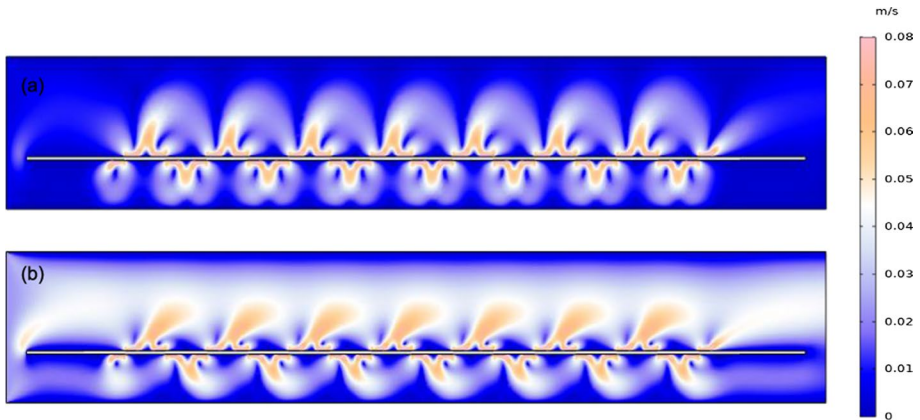
Fig. 6 Simulated flow pattern of the sDBD using a volume force of 3 kN/m^3 and flow of **a** 1 slm and **b** 5 slm N$_2$ (Color figure online)

where $\alpha_+(\lambda)$ and $\alpha_n(\lambda)$ are the polarizabilities of ions and neutrals, ρ_+, ρ_n and ρ_e the densities of ions, neutrals and electrons, λ, c_0, light wavelength, light velocity, ϵ_0, m_e and the permittivity, mass, and charge of an electron, respectively [18]. Equation (2) can be expanded to more species to describe a plasma more precisely. Due to the low degree of ionization, the contribution of the charged species can be neglected in the first order. In addition, due to the minimal CO$_2$ admixture, only the static polarizability of N$_2$ of 1.72×10^{-30} m^3, N atoms and 400 ppm concentration of CO$_2$ as, 1.1×10^{-30} m^3 and 2.64×10^{-30} m^3 [24, 25] is used in Eq. (2).

The contrast ϵ_x in the Schlieren image corresponds to the spatial derivative of the refractive index in Eq. (2) in x direction parallel to the sDBD (perpendicular to the knife edge direction in the experiment) that is integrated along the optical path z through the discharge:

$$\epsilon_x = \frac{1}{n} \int \frac{\partial n}{\partial x} dz \tag{3}$$

Results and Discussion

Power Absorption

Figure 7 shows the dissipated power in the sDBD for a flow of nitrogen of 1, 2, 5 slm with one percent admixture of carbon dioxide for varying peak-to-peak voltage of 6, 7, 8, 9, and 10 kV at 4 kHz repetition frequency of the high voltage bursts. In the most simple case, the scaling of the dissipated power in a dielectric barrier discharge should follow a linear scaling based on the analysis of an equivalent circuit model by Manley [26]. However, in practice, many different scalings can also be observed due to only partial coverage of the electrodes by plasma, especially at low voltages. In addition, depending on the excitation scheme, a varying degree of filamentation of the plasma may induce different scalings of power versus voltage. This can be accounted for by more elaborate equivalent circuit

Fig. 7 Absorbed power in the plasma versus applied peak-to-peak voltage for a one percent admixture of carbon dioxide to nitrogen. The solid line indicates a parabolic scaling
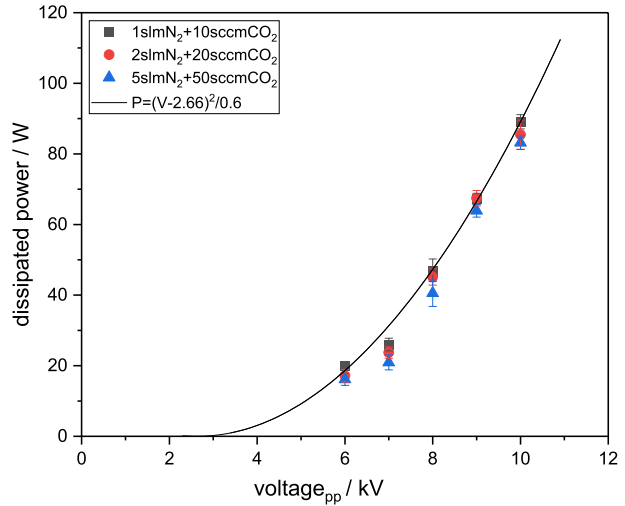
models [27]. In the end, a more general approach has been established to use a scaling according to [14, 28]:

$$P \propto (V - V_0)^n \quad 2 < n < 3 \tag{4}$$

This scaling was used to fit the data in Fig. 7 yielding an exponent $n = 2$ and an offset voltage $V_0 = 2.66$ kV. The observation of scaling with an exponent 2 might be explained by the expansion of the plasma filaments along the dielectric at higher powers, as described in detail by Pipa et al. [29]. One could also see that the power absorption in the setup does not depend on the gas flow.

Flow Pattern

The plasma-induced flow pattern is analyzed by comparing Schlieren measurements and simulations for a plasma operated at 10 kV peak-to-peak voltage with a burst frequency of 100 kHz being repeated at a frequency of 4 kHz for 1, 2, 5 slm nitrogen. Without the plasma, the flow pattern appears to be laminar and homogeneous in the Schlieren images. Figure 8 shows the measured Schlieren images for constant plasma power at $V_{pp} = 10$ kV at a varying gas flow rate of 1, 2, and 5 slm, respectively (top row in Fig. 8). The second row shows the simulated Schlieren images using a volume force of 3 kN/m³ for the same gas flow rates. The third row shows the velocity fields from the simulations. Small arrows emphasize the direction of the flow. The dashed yellow lines mark the location of the electrodes in Fig. 8.

The measured and simulated Schlieren images agree well, especially directly above the electrodes, where the refractive index gradient is the largest. One may see that both surface discharges starting from the electrode edges (indicated by 1 and 2 in Fig. 8a) meet each other and lead to the formation of upstream and downstream vortices with dark and bright patterns in the image (Fig. 8a).
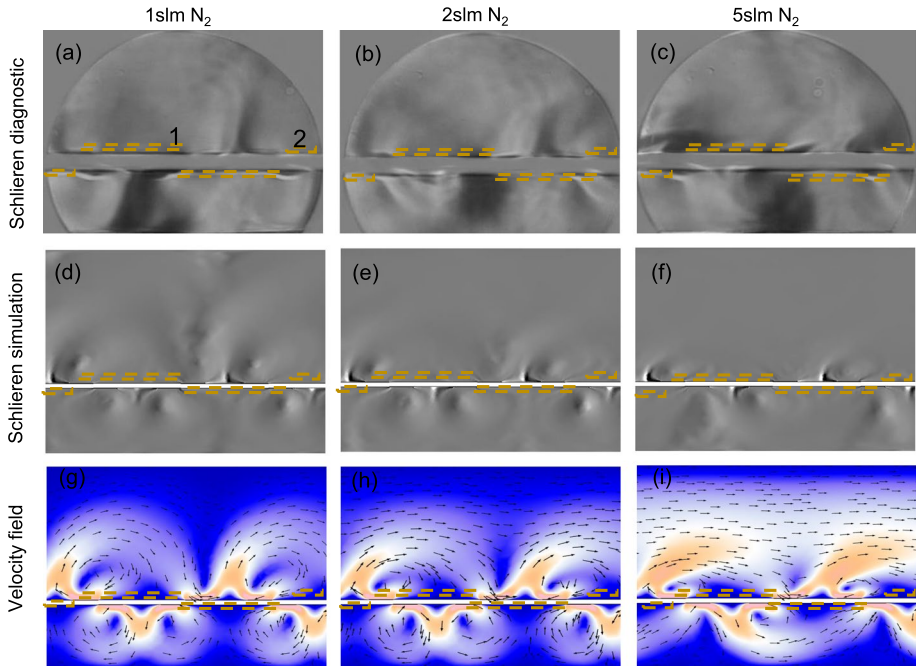
Fig. 8 Flow pattern for $V_{pp} = 10$ kV, $f = 4$ kHz as measured (**a**–**c**) and simulated (**d**–**f**) as well as the velocity fields (**g**–**i**) for gas flows of 1 slm, 2 slm, and 5 slm N_2. The dashed yellow lines mark the location of the electrodes

At larger distances to the electrodes, the Schlieren images become rather faint. Therefore, we extract the details of the flow pattern for this region more from the fluid simulations. From these, one can clearly see the formation of vortices above the electrode, which expand further into the volume at low flow rates. This is easy to understand since the surface discharge's volume force counteracts the chamber's overall gas flow. If the gas flow is high, the vortices become relatively small, because the volume force by the plasma cannot so easily compete with the momentum transfer from the gas flow through the reactor. This is discussed in the following:

In Fig. 8a and d, the measured and modeled Schlieren images for a mean flow velocity of 0.0034 m/s (flow 1 slm) are shown. One can clearly see that the flow pattern in the experiment can be reproduced in the simulation. The velocity field from the simulation in Fig. 8g, shows vortices that are created in the vicinity of the electrodes, as emphasized by streamlines. The overlap of vortices creates the different velocity regions illustrated in Fig. 8g—the bright region with high velocity and the dark blue color marks a low-speed region. The color bar is as same as shown in Fig. 6.

In Fig. 8b and e, the measured and modeled Schlieren image for a mean flow velocity of 0.009 m/s (flow 2 slm) is shown. Again, a very good agreement between experiment and simulation is found.

In Fig. 8c and f, the measured and modeled Schlieren image for a mean flow velocity of 0.023 m/s (flow 5 slm) is shown for an experiment using 5 slm of gas flow. One can see in the Schlieren image in Fig. 8c that the upstream and downstream vortices are almost absent since the incoming flow dominates the flow pattern direction(following the arrows).

Based on the simulated velocity fields in Fig. 8g, h, and i, one can state that the incoming flow bends the vortices towards the electrodes and prevents the vortices from expanding into the reactor volume, especially at higher flows. As a result, the height of these vortices gets smaller.

One might argue, however, that such a pattern might also be induced by simply heating effects of the plasma [30–32]. This is investigated by comparing the flow pattern at a boundary temperature of the electrode of room temperature of 293 K and at 340 K in the simulations showing no distinct impact on the flow pattern (not shown).

The effect of the applied voltage on the Schlieren pattern is presented in the first row in Fig. 9 for peak-to-peak voltages V_{pp} of 8, 9 and 10 kV and a flow of 2 slm N_2. The second row in Fig. 9 shows artificial Schlieren images from the simulation for a volume force of 1, 2, and 3 kN/m^3 at the same mean flow velocity. The third row in Fig. 9 shows the velocity field from the simulations. Following the sequence of images in Fig. 9a–c, one can see that an increase in the voltage and, thus the volume force from surface discharges counteracts the incoming gas flow by pushing the upstream and downstream vortices toward the volume and enhance, thereby, the gas mixing.

The formation of these vortices corresponds to an efficient mechanism for plasma gas mixing by pulling the incoming flow into the plasma region close to the electrode. The efficiency of this gas mixing can be defined by the extension of the vortex into the gas volume. Simulations quantify this by inspecting the velocity field images. Figure 10 shows simulated velocity fields and artificial Schlieren images for volume forces of 1000 and 3000 N/m^3 and varying mean flow velocities of 0.004 m/s, 0.009 m/s, and 0.023 m/s. From the
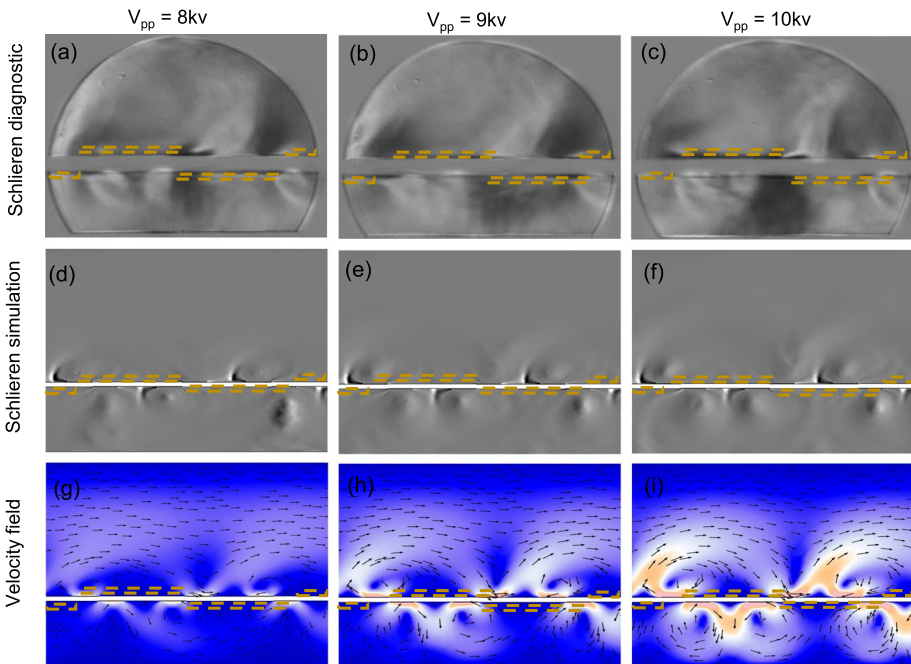
Fig. 9 Measured (**a–c**) and simulated Schlieren images (**d–f**) and velocity fields (**g–i**) for experiments using V_{pp} of 8, 9, 10 kV at a flow of 2 slm N_2
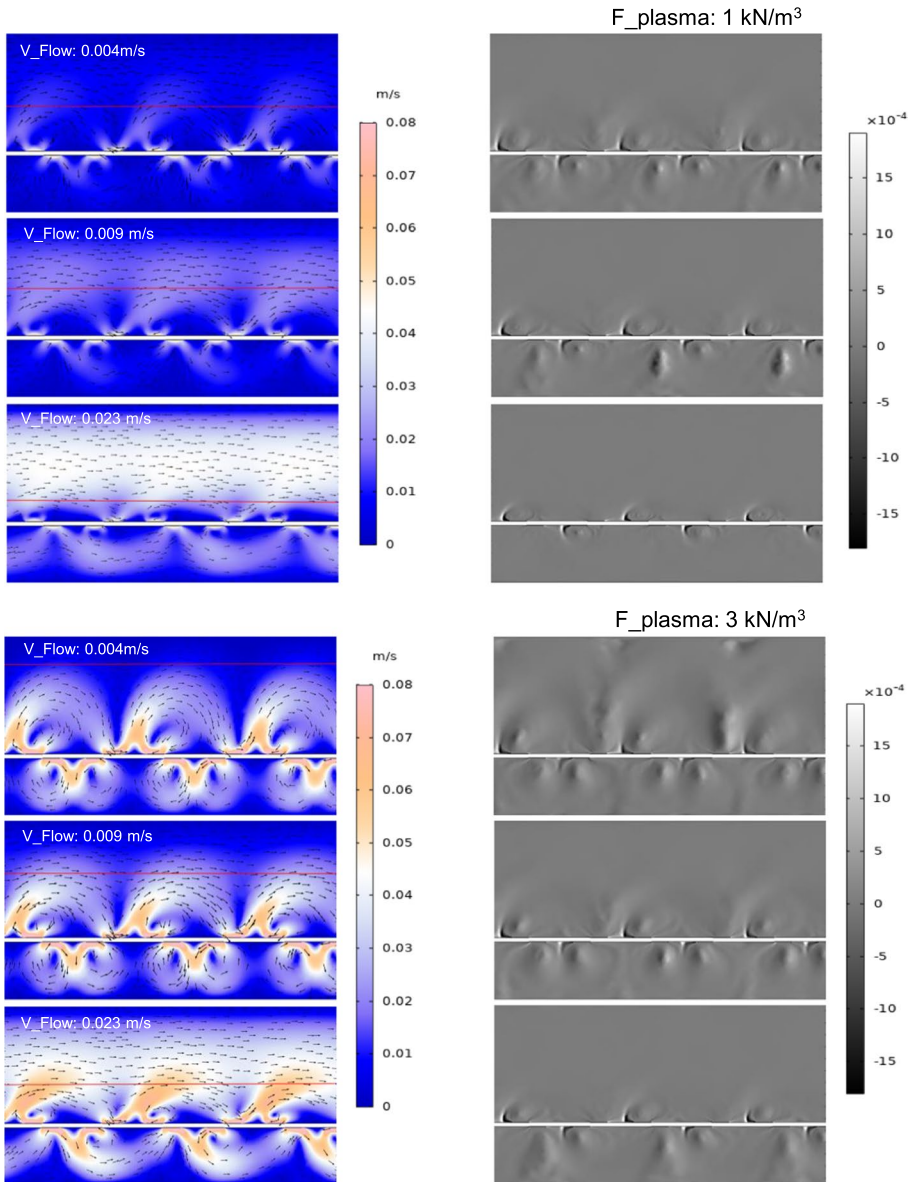
Fig. 10 Evolution of the plasma pattern expressed as velocity field (left) and as Schlieren simulation (right) at different mean flow velocities. The plasma volume force is assumed to be 1 and 3 kN/m³. The red cut line in the velocity field images determines the height of the vortices. The depicted geometry for all images is 3 cm in height and 7 cm in width (Color figure online)

images, it can be seen that the mean flow velocity is changing the vortex structure and thus the flow pattern. The height of the vortices has been estimated by following the outermost arrows of a vortex in the velocity field images (marked as a red line in Fig. 10). The largest distance from the electrode defines the height of the vortex.

The enhancement of the mixing between plasma and the gas stream by these vortices can be regarded as similar to the concept presented by Timmermann et al. [33] using a third electrode to induce an ion wind that drags reactive species from the plasma into the passing gas flow. The vortex-induced gas mixing, as presented here, can be regarded as equivalent because the ion wind in the plasma filament itself generates a vortex, which in turn enhances the mixing between gas flow and plasma species.

Plasma Conversion

The efficiency of the plasma-based species conversion in the sDBD and its dependence on the gas flow rate and plasma power is tested for splitting of CO_2 being admixed to 0.7% in nitrogen.

Figure 11 shows the temporal variation of the CO_2, CO, and N_2O density, as measured by FTIR during the plasma process using 0.7% CO_2 in N_2 and a peak-to-peak voltage of $V_{pp} = 10$ kV and a flow of 1 slm. The plasma was switched on at 32 min and switched off at 47 min. It can be seen that CO_2 is dissociated into CO and a small concentration of N_2O is also visible. The latter originates from the reaction of O with N_2. No other species could be detected in the FTIR spectra or may be below the detection limit. If one regards the absolute numbers, one sees that the depletion of CO_2 is almost the same as the formation of CO. The residual difference may be due to other $C_xN_yO_z$ species being below the detection limit of the FTIR since no carbon deposits on the electrodes are observed. The mass balance of oxygen, however, shows that only a small fraction of the O atoms originating from CO_2 dissociation react with the abundant N_2 to form N_2O. This is reasonable since the rate coefficient for three body O recombination is of the order of $1.07 \cdot 10^{-33}$ cm^{-6}s^{-1}[34], whereas the rate coefficient for the recombination of N_2 and O is of the order $5.02 \cdot 10^{-38}$ cm^{-6}s^{-1}[35]. Therefore, despite a large dilution of N_2 most of the O may recombine with CO or O back to CO_2 or O_2 which is not visible to the infrared spectrometer.

Based on these data, we assume that CO_2 molecules that enter the plasma filaments adjacent to the electrode are dissociated by electron impact, similar to the reaction sequence in pure CO_2 DBD discharges. The large dilution in nitrogen leads to a smaller

Fig. 11 Molar fractions of CO_2, CO and N_2O measured during an experiment using 0.7% CO_2 in N_2 and a peak-to-peak voltage of $V_{pp} = 10$ kV and a flow of 1 slm. The plasma was switched on at 30 min and switched off at 45 min. The dashed line marks the reference CO_2 admixture level in the feed gas in this experiment of 0.66%
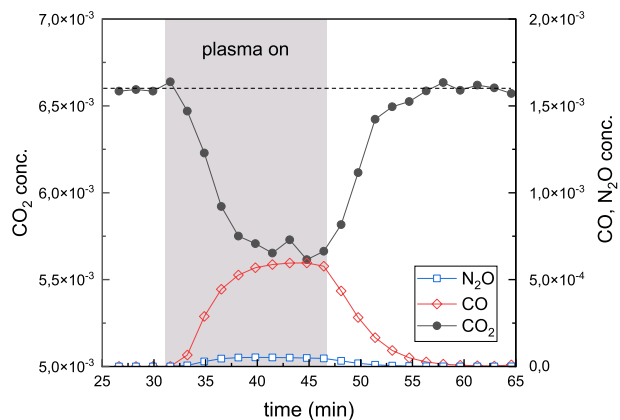
contribution of secondary reactions such as the reaction of O with O, CO, and CO_2. The dilution in nitrogen might also have a beneficial effect since the vibrational energy transfer from nitrogen to CO_2 is very efficient so that the rate for electron-induced dissociation of CO_2 might be larger due to the vibrational excitation of CO_2. This will be a topic of future research. Most important, however, is the fact that the conversion of CO_2 depends not only on the plasma properties of the DBD plasma itself but also on the efficiency of the transport of CO_2 from the gas stream into the plasma region.

The conversion χ of CO_2 is defined as:

$$\chi = \left(1 - \frac{C_{outlet}}{C_{inlet}} \right) \qquad (5)$$

with C_{outlet} and C_{inlet} being the concentrations of CO_2 with plasma on and off. The conversion is quantified for different specific energy inputs (SEI). The SEI is defined as:

$$SEI[kJ/L] = \frac{P[kW]}{\Phi[L/s]} \qquad (6)$$

with P the absorbed power and Φ the gas flow.

Figure 12b shows the conversion versus SEI conversion. At first glance, the typical behavior as it is known for many plasma chemistry systems, is observed as the conversion increases until it saturates for increasing SEI. This would be consistent with regular plasma-based conversion of CO_2 showing a decrease in conversion for increasing the gas flow rate [36, 37]. This saturation is usually either at 100% indicating complete conversion or at a characteristic value below 100% when a dissociation reaction's forward and back reactions are in equilibrium. In our experiment, however, only 15% conversion can be reached and any backreaction can be excluded since our test molecule CO_2 is heavily diluted in N_2. The low conversion in our sDBD design may be explained by the fact that a large fraction of CO_2 bypasses the plasma region explaining the saturation of the conversion already at low values of 15%. This leads to the hypothesis that the characteristic scaling of the conversion with SEI is not induced by the plasma chemistry alone, but also by the efficiency of the vortex-based plasma-gas mixing in our setup. This is different from conventional volume DBDs where a perfect mixing of plasma and gas is assured since the gas has to pass a narrow discharge gap.

This is analyzed by quantifying the efficiency of the plasma-gas mixing using the heights of the vortices from the simulation, as shown in Fig. 12a. These can be directly compared to the conversion versus SEI data, by using an equivalent scaling parameter from the simulations. For this, we selected the volume force F by the plasma exerted on the gas stream divided by the mean flow velocity. This should be proposed to the SEI because the volume force is selected to be proportional to the plasma power and the mean flow velocity is proportional to the flow rate. The exact correlation is based on the analysis of the

Table 1 Scaling of the force in the simulation with the applied voltage and power in the experiment yielding a similar flow pattern

Plasma force in simulation [N/m³]	Plasma power in experiment [W]	V_{pp} [kV]
1000	45 ± 3.08	8
2000	67 ± 1.86	9
3000	85 ± 2.68	10

Fig. 12 **a** Height of the vortex depending on plasma volume force, **b** conversion of CO_2 depending on the specific energy input (SEI)
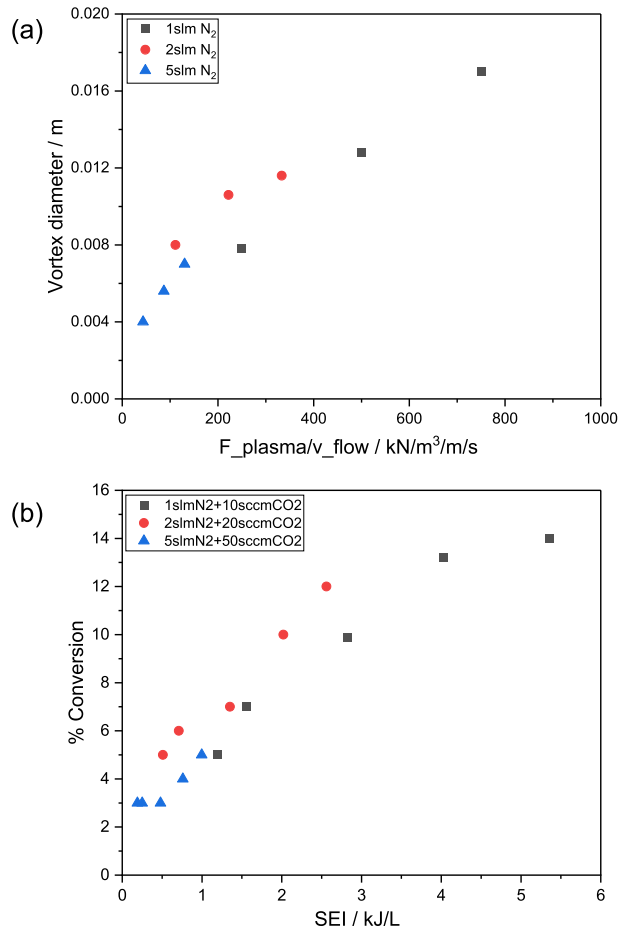
experiment's Schlieren images and the fluid simulations' flow pattern. Thereby, the plasma force in the simulation can be connected to the plasma power or peak-to-peak voltage for the same mean flow velocity, as listed in Table 1. Based on this comparison a volume force of 3000 N/m³ at a gas flow of 1 slm (= 750 kN/m³/m/s) yields a simulated Schlieren image that is very similar to the measured Schlieren pattern in an experiment using 86 W absorbed plasma power at the same gas flow corresponding to SEI of 5.16 kJ/l. This correlation is used to align the *x*-axes in Fig. 12a and b. One can see that the saturation behavior of the SEI is identical to the saturation behavior of the heights of the vortices. These vortices saturate in height because they fill above a certain force per mean flow velocity the complete cross-section of the reactor chamber. In summary, one may state that the saturation behavior of the SEI is not created by the complete depletion of the source gas molecules, but rather by a saturation of the mixing efficiency of the plasma actuator-driven gas vortices.

Despite perfect mixing, when the vortices are as large as the reactor volume, a conversion of only 15% is reached. This may be caused by the limited conversion of CO_2 molecules passing the plasma volume directly above the electrode. We can even speculate that the dissociation of CO_2 directly inside the plasma may not be affected by the varying

plasma power, because an increasing plasma power also induces an increase in the local mean flow velocity within the plasma so that the dissociation efficiency inside the plasma itself (being the ratio between absorbed power and flow) could stay constant. This is different from volume DBDs, where the force exerted by the streamer on the gas is perpendicular to the gas flow. In the case of the plasma actuator design, the gas is accelerated at higher plasma powers, so that the residence time decreases.

The crucial role of the plasma-induced flow pattern in gas conversion is identified as vortex formation in the vicinity of the surface discharges. The interaction of upstream and downstream flows creates the vortices. The incoming flow is pulled into these vortices but also bends them toward the surface. Therefore, the incoming flow velocity also regulates the height of these vortices.

Conclusion

The combination of plasma-based species conversion and plasma-based flow control is studied in a surface dielectric barrier discharge. The flow patterns were recorded by the Schlieren imaging technique, and the species concentrations by infrared spectroscopy. It is observed that characteristic vortices are formed that enhance the plasma gas mixing and species conversion. In the future, more elaborate plasma models will be required to calculate the plasma force on the flow directly. Furthermore, plasma electrode designs like different comb designs or stacks of electrodes need to be explored to optimize the flow control concerning the efficiency of species conversion.

Author Contributions SM performed the experiments, simulation, interpretation, and manuscript writing. AvK provided the experiment idea, data interpretation, project concept, and manuscript editing.

Availability of data and materials The authors can provide all data upon reasonable request.

Declarations

Conflict of interest No conflict of interest on behalf of all authors.

References

1. Kogelschatz U (2003) Dielectric-barrier discharges: their history, discharge physics, and industrial applications. Plasma Chem Plasma Process 23:1–46
2. Bogaerts A, Berthelot A, Heijkers S, Kolev S, Snoeckx R, Sun S, Trenchev G, Van Laer K, Wang W (2017) CO_2 conversion by plasma technology: insights from modeling the plasma chemistry and plasma reactor design. Plasma Sources Sci Technol 26:063001
3. Navascués P, Cotrino J, González-Elipe AR, Gómez-Ramírez A (2022) Plasma assisted CO_2 dissociation in pure and gas mixture streams with a ferroelectric packed-bed reactor in ambient conditions. Chem Eng J 430:133066
4. Mei D, He Y-L, Liu S, Yan J, Tu X (2016) Optimization of CO_2 conversion in a cylindrical dielectric barrier discharge reactor using design of experiments: optimization of CO_2 conversion. Plasma Process Polym 13:544–556
5. Ozkan A, Bogaerts A, Reniers F (2017) Routes to increase the conversion and the energy efficiency in the splitting of CO_2 by a dielectric barrier discharge. J Phys D Appl Phys 50:084004
6. Stewig C, Schüttler S, Urbanietz T, Böke M, von Keudell A (2020) Excitation and dissociation of CO_2 heavily diluted in noble gas atmospheric pressure plasma. J Phys D Appl Phys 53:125205
7. Kogelheide F, Offerhaus B, Bibinov N, Krajinski P, Schücke L, Schulze J, Stapelmann K, Awakowicz P (2020) Characterisation of volume and surface dielectric barrier discharges in $N_2 - O_2$ mixtures using optical emission spectroscopy. Plasma Processes Polym 17:1900126
8. Ollegott K, Peters N, Antoni H, Muhler M (2019) Catalytic carbon monoxide oxidation over potassium-doped manganese dioxide nanoparticles synthesized by spray drying. Emiss Control Sci Technol 5:378–391
9. Schücke L, Gembus J-L, Peters N, Kogelheide F, Nguyen-Smith RT, Gibson AR, Schulze J, Muhler M, Awakowicz P (2020) Conversion of volatile organic compounds in a twin surface dielectric barrier discharge. Plasma Sources Sci Technol 29:114003
10. Schücke L, Bodnar A, Friedrichs N, Böddecker A, Peters N, Ollegott K, Oberste-Beulmann C, Wirth P, Nguyen-Smith RT, Korolov I, Gibson AR, Muhler M, Awakowicz P (2022) Optical absorption spectroscopy of reactive oxygen and nitrogen species in a surface dielectric barrier discharge. J Phys D Appl Phys 55:215205
11. Nguyen-Smith RT, Böddecker A, Schücke L, Bibinov N, Korolov I, Zhang Q-Z, Mussenbrock T, Awakowicz P, Schulze J (2022) μs and ns twin surface dielectric barrier discharges operated in air: from electrode erosion to plasma characteristics. Plasma Sources Sci Technol 31:035008
12. Böddecker A, Bodnar AA, Schücke L, Giesekus J, Wenselau K, Nguyen- Smith RT, Oppotsch T, Oberste-Beulmann C, Muhler M, Gibson AR, Awakowicz P (2022) A scalable twin surface dielectric barrier discharge system for pollution remediation at high gas flow rates. React Chem Eng 7:2348–2358
13. Ollegott K, Wirth P, Oberste-Beulmann C, Sakthi GSM, Magazova A, Hermanns P, Peters N, Schücke L, Bracht V, Agar DW, Awakowicz P, Muhler M (2023) Investigation of flow characteristics in a twin-surface dielectric barrier discharge reactor by Schlieren imaging. J Phys D Appl Phys 56:265201
14. Enloe CL, McLaughlin TE, VanDyken RD, Kachner KD, Jumper EJ, Corke TC (2004) Mechanisms and responses of a single dielectric barrier plasma actuator: plasma morphology. AIAA J 42:589–594
15. Leonov SB, Adamovich IV, Soloviev VR (2016) Dynamics of near-surface electric discharges and mechanisms of their interaction with the airflow. Plasma Sources Sci Technol 25:063001
16. Sato S, Furukawa H, Komuro A, Takahashi M, Ohnishi N (2019) Successively accelerated ionic wind with integrated dielectric-barrier-discharge plasma actuator for low-voltage operation. Sci Rep 9:5813
17. Moreau E, Louste C, Touchard G (2008) Electric wind induced by sliding discharge in air at atmospheric pressure. J Electrostat 66:107
18. Traldi E, Boselli M, Simoncelli E, Stancampiano A, Gherardi M, Colombo V, Settles GS (2018) Schlieren imaging: a powerful tool for atmospheric plasma diagnostic. EPJ Tech Instrum 5:4
19. Damen MA, Martini LM, Engeln R (2020) Temperature evolution in a pulsed $CO_2 - N_2$ glow discharge measured using quantum cascade laser absorption spectroscopy. Plasma Sources Sci Technol 29:065016
20. ...Rothman L, Gordon I, Barbe A, Benner D, Bernath P, Birk M, Boudon V, Brown L, Campargue A, Champion J-P, Chance K, Coudert L, Dana V, Devi V, Fally S, Flaud J-M, Gamache R, Goldman A, Jacquemart D, Kleiner I, Lacome N, Lafferty W, Mandin J-Y, Massie S, Mikhailenko S, Miller C, Moazzen-Ahmadi N, Naumenko O, Nikitin A, Orphal J, Perevalov V, Perrin A, Predoi-Cross A, Rinsland C, Rotger M, Šimečková M, Smith M, Sung K, Tashkun S, Tennyson J, Toth R, Vandaele A, Vander Auwera J (2009) The HITRAN 2008 molecular spectroscopic database. J Quant Spectrosc Radiat Transf 110:533–572

21. Bouchmal A (2011) Modeling of dielectric-barrier discharge actuator. PhD thesis (Delft University)
22. Suzen Y, Huang G (2006 Jan) Simulations of flow separation control using plasma actuators. In: 44th AIAA aerospace sciences meeting and exhibit
23. Lai C, Fu H, Bo H, Ling Z, Jiang L (2020) Aerodynamic drag reduction and optimization of MIRA model based on plasma actuator. Actuators 9:64
24. Thole B (1981) Molecular polarizabilities calculated with a modified dipole interaction. Chem Phys 59:341–350
25. Alms GR, Burnham A, Flygare WH (1975) Measurement of the dispersion in polarizability anisotropies. J Chem Phys 63:3321–3326
26. Manley T (1943) The electric characteristics of the ozonator discharge. Trans Electrochem Soc Elektorchem Soc 84:83
27. Brandenburg R, Schiorlin M, Schmidt M, Höft H, Pipa AV, Brüser V (2023) Plane parallel barrier discharges for carbon dioxide splitting: influence of discharge arrangement on carbon monoxide formation. Plasma 6:162–180
28. Forte M, Jolibois J, Pons J, Moreau E, Touchard G, Cazalens M (2007) Optimization of a dielectric barrier discharge actuator by stationary and nonstationary measurements of the induced flow velocity: application to airflow control. Exp Fluids 43:917–928
29. Pipa AV, Hink R, Foest R, Brandenburg R (2020) Dependence of dissipated power on applied voltage for surface barrier discharge from simplest equivalent circuit. Plasma Sources Sci Technol 29:12LT01
30. Park S, Cvelbar U, Choe W, Moon SY (2018) The creation of electric wind due to the electrohydrodynamic force. Nat Commun 9:371
31. Boeuf JP, Lagmich Y, Unfer T, Callegari T, Pitchford LC (2007) Electrohydrodynamic force in dielectric barrier discharge plasma actuators. J Phys D Appl Phys 40:652–662
32. Qu J, Zeng M, Zhang D, Yang D, Wu X, Ren Q, Zhang J (2022) A review on recent advances and challenges of ionic wind produced by corona discharges with practical applications. J Phys D Appl Phys 55:153002
33. Timmermann E, Prehn F, Schmidt M, Höft H, Brandenburg R, Kettlitz M (2018) Indoor air purification by dielectric barrier discharge combined with ionic wind: physical and microbiological investigations. J Phys D Appl Phys 51:164003
34. Tsang W, HRF (1986) CO + O * M > CO2 + M. J Phys Chem Ref Data 15
35. Schofield K (1973) Evaluated chemical kinetic rate constants for various gas phase reactions. J Phys Chem Ref Data 2:25
36. Aerts R, Somers W, Bogaerts A (2015) Carbon dioxide splitting in a dielectric barrier discharge plasma: a combined experimental and computational study. ChemSusChem 8:702–716
37. Xu S, Khalaf PI, Martin PA, Whitehead JC (2018) CO_2 dissociation in a packed-bed plasma reactor: effects of operating conditions. Plasma Sources Sci Technol 27:075009